Visualization of Bubble Formation in Porous Media

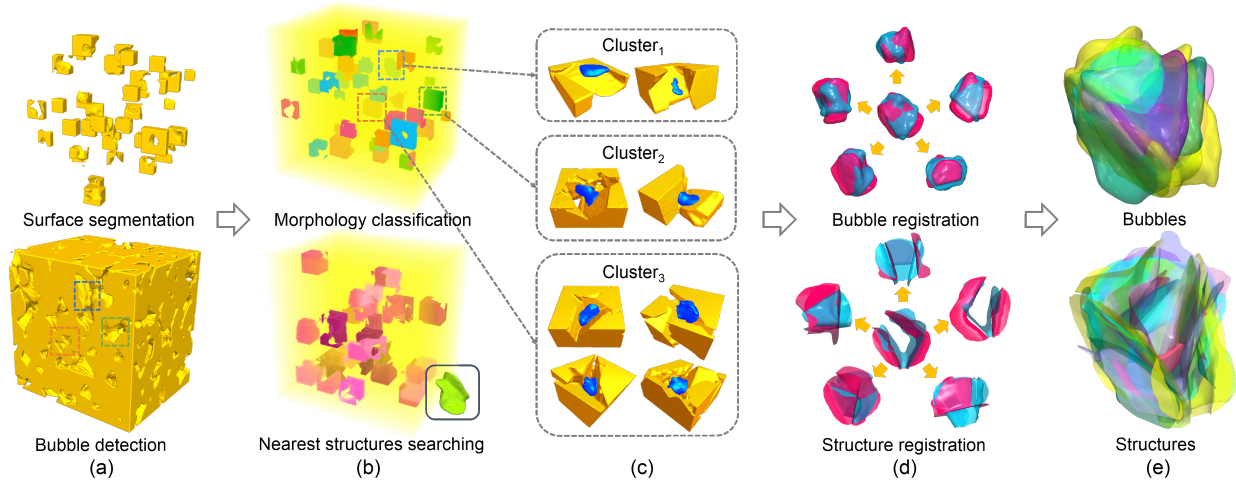Hui Zhang, Steffen Frey, Holger Steeb, David Uribe, Thomas Ertl, and Wenping Wang

Fig. 1: Overview of our visualization approach for analyzing bubble formation in porous media. (a) Detection of bubbles in a porous medium and extraction of porous structures (Sect. 3); (b) morphology-based bubble classification (top: colors indicate different clusters) (Sect. 4.1) and identification of similar structures for a bubble of interest (bottom: brightness of pink denotes similarity to the structure of the green bubble) (Sect. 4.2); (c) clustering of bubbles (blue) according to their connectivity to the surrounding structure (yellow); (d) registration of bubbles and structures, shown from six different views (Sect. 5); (e) integrated visualization of multiple bubbles and structures (bubble and corresponding structure are depicted in the same color, Sect. 6).

Abstract—We present a visualization approach for the analysis of CO_2 bubble-induced attenuation in porous rock formations. As a basis for this, we introduce customized techniques to extract CO_2 bubbles and their surrounding porous structure from X-ray computed tomography data (XCT) measurements. To understand how the structure of porous media influences the occurrence and the shape of formed bubbles, we automatically classify and relate them in terms of morphology and geometric features, and further directly support searching for promising porous structures. To allow for the meaningful direct visual comparison of bubbles and their structures, we propose a customized registration technique considering the bubble shape as well as its points of contact with the porous media surface. With our quantitative extraction of geometric bubble features, we further support the analysis as well as the creation of a physical model. We demonstrate that our approach was successfully used to answer several research questions in the domain, and discuss its high practical relevance to identify critical seismic characteristics of fluid-saturated rock that govern its capability to store CO_2.

Index Terms—3D volume rendering, bubble visualization, porous media

---

◆

---

1 INTRODUCTION

Carbon dioxide storage in subsurface geologic formations is one option to reduce significant levels of CO_2 emitted to the atmosphere [19]. For this, carbon dioxide is stored in permeable sandstone reservoir by injecting supercritical CO_2 into water-saturated porous sandstone formations. The injection process is performed under controlled pressure-temperature conditions and depicted as CO_2 sequestration [42]. Carbon dioxide has been injected safely into subsurface reservoirs for many

- *Hui Zhang and Wenping Wang are with the Department of Computer Science at The University of Hong Kong. E-mail: {hzhang|wenping}@cs.hku.hk.*
- *Steffen Frey and Thomas Ertl are with the Visualization Research Center of the University of Stuttgart.*
  E-mail: {steffen.frey|thomas.ertl}@visus.uni-stuttgart.de.
- *Holger Steeb and David Uribe are with the Institute of Applied Mechanics at the University of Stuttgart.*
  E-mail: {holger.steeb|david.uribe}@mechbau.uni-stuttgart.de.

years for Enhanced Oil Recovery [5]. Fundamental science and engineering principles indicate that CO_2 sequestrated systems should be feasible and safe: the energy cost of preparing CO_2 for injection can be as low as a few percent of the heating value of the original fuel. However, long-term CO_2 storage does carry a risk of possible leaks to the atmosphere and, in addition, subsequent hydro-chemical processes could lead to an evolution of thermodynamical conditions. The costs and risks are not insurmountable, but research is required to make these concepts economically and technologically feasible. It was recently shown [7] that local wave scattering, e.g. caused by resonance effects, affects the effective velocity dispersion and intrinsic attenuation of fluid-saturated porous media. In order to predict the behaviour of geological formations or to identify the properties of the subsoil in seismic prospecting methods, more realistic coarse-grained continuum models have to be developed taking into account relevant pore-scale effects like bubble resonance.

In this paper, we concern ourselves with visualizing CO_2-bubbles which are de-gased from the pore-fluid (water) caused by disturbed thermodynamical conditions, i.e. a decrease of the pressure state [27, 28, 34, 35]. Even a small volume fraction of gas bubbles changes effective coarse-grained seismic properties (wave dispersion and atten-

uation) drastically [7, 23]. Related abnormal velocity dispersion and attenuation phenomena could be used in reservoir monitoring as a new evidence for the amount of de-gased CO2 and therefore as a "leakage" indicator. Local resonance effects of single CO_2 bubbles depend on several (geometrical) factors like the volume of the CO_2 bubbles, their specific geometrical shape and their trapping conditions, i.e. the local morphology of the surrounding pore space. Image-based direct numerical simulations of bubble resonance properties are a challenging task, as necessary geometrical information of local bubbles and bubble distribution in the rock is missing [17], [18]. High-resolution XCT scans performed under controlled pressure-temperature conditions as the ones we will discuss here, are very rare. Still, a physical-based pore-scale interpretation of these phenomena is missing and could only be achieved by a detailed bottom-up characterization of the involved properties on the bubble or pore scale of the porous media.

In a collaborative effort of visualization and domain scientists, we designed a visualization-based analysis approach that allows us to address this. Instead of only observing the effect on a general macroscale, we propose to visually study individual CO_2 bubbles in the context of their local corresponding structures to understand fundamental, small-scale characteristics, patterns, and properties. Most research questions revolve either directly or indirectly around the formation of individual CO_2 bubbles in the porous material. Below we list the most critical research questions **RQ 1-4** derived either directly or indirectly around the formation of individual CO_2 bubbles in the porous media that needed to be handled, and provide background to motivate why they are of crucial interest in the domain:

RQ1 (bubble locations) Where do bubbles form in porous media?
Knowing the potential positions of (gas) bubbles in the pore space allows for a potential estimate about the numbers (and locations) of bubbles in a unit cell. If possible bubble locations are known, generic worst case scenarios with the maximum numbers of bubbles could be performed (highest amount of attenuation).

RQ2 (bubble size distribution) What is the bubble size distribution?
The bubble size is directly linked to the resonance frequency of a single bubble, cf. phase velocity depicted in Figure 11. Elasto-dynamical simulations taking into account the shape of the bubble and the morphology of the surrounding pore structure provide realistic resonance properties. If we know the bubble size distribution in a unit cell, we could additionally calculate the distribution of resonance frequencies and the coarse-grained dispersive characteristics like e.g. phase velocities and attenuation (cf. [7, 25]).

RQ3 (structure influence on bubble) What kind of (governing) boundary conditions for bubbles exist?
In porous geomaterials like sandstone, we expect that bubbles have a non-spherical geometry, and are potentially attached to one or more solid surfaces. Pinned bubbles or bubbles attached to the surface of the pores, have different resonance frequencies (eigenmodes) compared to free, i.e. non-attached bubbles. These eigenforms/eigenfrequencies can not be calculated analytically anymore and need sophisticated numerical modeling and simulations of boundary value problems.

RQ4 (bubble from structure) Can we determine from the pore space morphology size and boundary conditions of bubbles?
If we have the link between pore space morphology and boundary conditions of bubbles, we would then extract bubble positions, sizes and boundary conditions, and directly perform numerical finite element calculations for the determination of resonance frequencies. Finding a link between pore space morphology and bubble size/location is challenging and strongly depends on the type of porous media. Nevertheless, such a link allows for high resolution XCT scans which are necessary for small bubble diameters and subsequent medium resolution scans for representative pore morphologies where potentially the bubbles can not be resolved.

To answer the above these research questions, we need to overcome a variety of visualization technical challenges. First of all, we work with high-resolution data derived from XCT which the size of data induces issues of data handling. A challenge on its own is the reconstruction of particularly the bubbles due to the small size in combination with measurement artifacts and noise in the XCT scan, as well as the low bubble structure contrast of the images overall. More importantly, in our analysis task, we have to obtain knowledge from the inside of a complex, dense porous medium structure. This means that any direct visualization technique would suffer from significant issues due to occlusion and visual clutter. While this in itself is already quite challenging, how to extract quantitative characteristics that represent the critical morphology and geometric structure features from digital images is also a challenge. All these aspects render standard volume visualization techniques mostly ineffective for addressing our research questions.**RQ4 (bubble from structure)** essentially addresses an ambitious long-term goal and addressing it could significantly advance research in the field, however, it us currently unclear to what extent and how this can be achieved. We can only begin to tackle this in the context of this paper, so in the context of this paper we rather provide a starting point for this investigation and a direction for future work.

To resolve these challenges and address our research questions, we present our approach for the visual analysis of CO_2 sequestration processes, that consists of the individual parts discussed below:

- we first detect and segment bubbles with their surrounding volumes from an XCT dataset (Sect. 3);

- we then classify bubbles into several clusters with respect to morphology (cf. Sect. 4.1) . . .

- . . . and propose an efficient approach to identify both similar porous medium structures and bubbles (Sect. 4.2 & Sect. 4.3);

- we propose a registration approach both for bubbles and structures to allow for a meaningful direct visual comparison (Sect. 5);

- we finally use our introduced techniques for the visual analysis of bubble formation and address our research questions (Sect. 6).

2 RELATED WORK

Visualization at material interfaces. A large body of work on material interface visualization concerns itself with the extraction of interfaces and presents information directly on these extracted surfaces. In particular, numerous works have been proposed in the context of volume fraction data in multi-fluid simulations. Meredith et al. [24] propose a new algorithm specifically for reconstructing material interfaces for visualization and visual analysis. For material interface reconstruction, Prilepov et al. [29] employ a patch-based gradient field approximation to generate a volume fraction function within each cell of the data set, which can be used to generate a smooth interface that preserves the respective volume fractions. Lindholm et al. [21] combine multiple classifiers to enhance the classification of different materials and their respective boundaries. In contrast to these visualization approaches which focus on extracted surfaces, we will pursue a more general and comprehensive approach by considering the volume in the vicinity of the interface.

Visualization of porous media. For analyzing defects in XCT data, Reh et al. [30] present MObects, an approach to explore a high number of individual objects in a data set, which is demonstrated in particular for analyzing pores in carbon fiber reinforced polymers. For the same application area, Weissenböck et al. [40] further propose a new visual analysis tool to interactively explore features of fiber properties. Grau et al. [10] presented a method to analyze pore connectivity inside rock formations, which supports the exploration of porous structures via illustrative visualization. Gyulassy [11] investigate the properties of a deforming porous structure based on topological features, and produce a skeleton representation to examine changes over time. Ushizima et al. [37] describe tools that provide measurements of porosity as well as permeability estimates using geometric and topological descriptors, and visualize pore structures and networks. On this basis, they discuss potentials of the material for fluid storage (and briefly touch upon CO_2 storage), yet, in contrast to this work, this is only based on the porous material itself and does not directly analyze actual bubble formations.
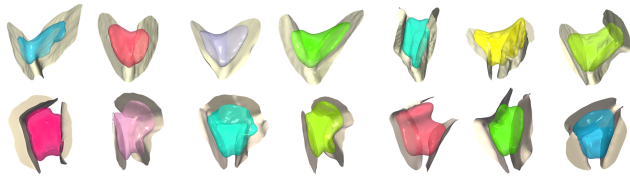
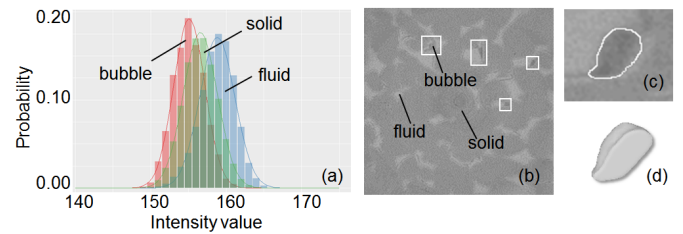Fig. 2: Extracted bubbles and structures (color denotes bubble id).

Fig. 3: Bubble detection and porous surface extraction. (a) Histogram of three phases in one bubble region of the XCT image. (b) Bubble detection (white rectangle) (Sect. 3(1)) and (c) precise segmentation (Fig. 3(2)). (d) Rendering of a 3D reconstruction.

Providing a overview on the topic, Heinzl et al. [12] give a comprehensive overview on visual computing in the domain of material science in general. Also, standard volume visualization techniques are widely used to analyze porous media data from simulations and measurements. Beyer et al. [4] review techniques for GPU-based volume visualization with a focus on the rendering of large-scale data. In the context of this project, large volumes of scalar data of varying precision will result from both XCT scans and simulations.

Focus+Context visualization. The core idea with focus+context visualizations is to enable viewers to see the object of primary interest presented in full detail while at the same time providing an overview of the surrounding information. Various techniques have been presented to account for the varying importance of different areas of the volume [38] and to simplify visualizations consisting of multiple components [3]. Wu and Popescu [41] present a framework for designing multi-perspective focus+context visualizations and adapt the camera to alleviate occlusions. Krüger et al. [16] derive features from images and focus their visualization on these while preserving contextual information. They also provide a point-and-click interface for interactively selecting and exploring structures in the data.

3D Shape Registration. 3D shape registration aims at putting multiple shapes into a common coordinate system to better understand their geometry. A common approach is to first find their correspondence by comparing shape features to estimate a coarse transformation matrix, followed by the Iterative Closest Point (ICP) algorithm [33] to further refine it. According to the regions that extract features, approaches may be classified into global and local methods. Global methods describe the character of the whole shape, for example, shape distributions [26] for rigid objects and Reeb graphs [14] for articulated objects. In contrast, local methods encode local shape features which can lead to finding more reliable correspondences Gelfand et al. [9] adopt the covariance matrix to constrain the eigenspace such that a set of points which affect both translation and rotation are used. Tombari et al. [36] propose a new 3D surface descriptor that conceptually combines two categories of methods, namely signatures and histograms. In this work, we employ a local registration approach on the basis of ICP that has explicitly been designed for good performance in our application scenario.

3 SEGMENTATION OF BUBBLES AND POROUS STRUCTURES

Our XCT dataset captures the CO_2 bubble sequestration process from an experiment in which fluid with gas is injected into a (porous) Fontainebleau sandstone under disturbed thermodynamical conditions. Our dataset has a resolution of $2560 \times 2560 \times 2160$ voxels with a resolution of $0.65\,\mu m$ per voxel. The radius of the bubbles typically ranges between $13\,\mu m$ and $26\,\mu m$ (i.e., around 20 to 40 in terms of voxels). While in the experiment several measures are taken to yield results with as high contrast as possible, bubble segmentation still is challenging and requires manual input by an expert for good results. In addition, the datasets are often reduced in both resolution and considered area to reduce computation time and artifacts (e.g. [1]). Recently, a complex mixed volume reconstruction method has been presented, where first the solid phase is taken care of, and then gas and fluid phases are segmented using a Paganin filter reconstruction [39]. However, in our experience, this results in unsharp phase boundaries which add high uncertainties in further computation steps.

In our work, to get an initial impression of the data, we manually labeled an XCT image slice and constructed the intensity histograms of the three phases: bubbles, fluid and solid porous structure (cf. Figure 3). Here, Gaussian curves are fitted to intensity values by calculating the mean and standard deviation of each phase. At this example, we see that most intensity values lie in a small value range (between 150 and 160 in our 16 bit resolution data). Despite all efforts to maximize the contrast in the setup of the experiment, this results in a particularly challenging problem for automatic bubble extraction. Below, we discuss our customized segmentation approach that runs automatically, yet still allows for manual adjustments by experts in certain phases to handle inadequate results. Our approach essentially consists of two steps, conceptually following the approach of Furukawa et al. [8]. We first detect regions of interest (ROI) in which bubbles occur using statistical segmentation [43] (1) and then carry out the precise segmentation within each ROI with a level set approach [20] (2).

(1) Bubble Detection and Feature Extraction. Given the XCT image slices as input, the first step of our method is to detect the ROI in which bubbles occur. For this, we employ a statistical segmentation method, which segments images by labeling voxels based on the intensity distribution of our three phases [43]. For initialization, we use k-means to cluster and label voxels accordingly in all the image slices into bubbles, fluid and solid structure. The intensity distribution is modeled by a Gaussian Mixture Model, whose parameters are iteratively estimated using an Expectation-Maximization algorithm (EM). The E-step labels pixels, while the M-step adjusts the Gaussian parameters considering the updated labels. This is repeated until the maximum iteration reached or algorithm converges (cf. [43] for a detailed discussion of this step). We then construct a bubble set $\mathcal{B}$. For this, we cluster coherent regions of bubbles, and create a respective ROI for each (e.g., similar to [43]). The ROI along each axis is twice the size of the bounding box around the bubble, and it is positioned such that the bubble is in its center. According to our experience, this suffices to meaningfully extracting the porous structures around a bubble. After this step, the results are manually checked, and incorrectly identified bubble ROIs are discarded.

(2) Segmentation and Surface Reconstruction. Next, solving our research questions requires accurate representations of the bubble and porous structures. We use a level set method to achieve this, as they can efficiently segment objects of both varying shape and intensity. Each level-set function represents one object (e.g., a bubble), and the evolution equation for each level-set function is derived using the variational approach, which yields good results for segmenting images with weak boundaries (please cf. [20] for a detailed discussion). We initialize the level-set function using the bubble bounding box of ROI (from step (1)). After the level-set function is converged, we conceptually obtain an isosurface that describes the boundary of the object. With the respective isovalue, we generate a triangle mesh using Marching Cubes [22] for both bubbles and structures.

4 MORPHOLOGY AND SIMILARITY

In this section, we present automatic analysis techniques that allow addressing different types of research questions. First, we analyze bubbles with respect to their morphology (cf. Sect. 4.1). Here, identifying the different types of bubbles occurring in the porous media along with their frequency is of high interest for the analysis. Next, for further investigation, we introduce an algorithm that can identify similar porous structures (cf. Sect. 4.2), which is particularly important to analyze the influence of a structure on the type of occurring bubble.
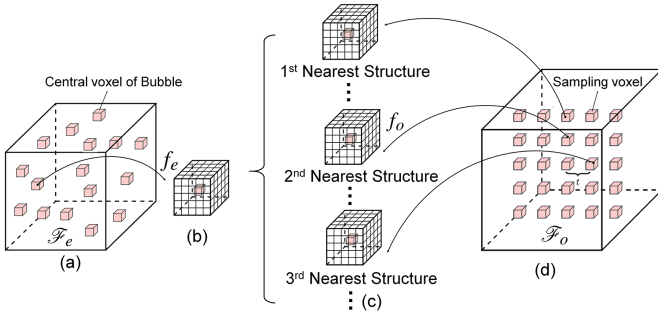
Fig. 4: Searching for nearest (i.e., most similar) structures in the porous medium. (a) The exemplar-structure feature set $\mathscr{F}_e$ consists of detected bubbles and their surrounding structures. (b) An extended neighborhood is considered with the exemplar-structure feature cube f_e. (c) Identify the most similar feature cubes f_o in the data by (d) comparing against the desired-structure feature set $\mathscr{F}_o$.

Akin to this, we also present an approach that, starting from a particular bubble of interest, enables us to find bubbles with similar geometric shape (cf. Sect. 4.3).

4.1 Morphology-based Bubble Classification

A crucial question for the overall analysis in the domain is to identify what kind of porous media are suitable for CO_2 storage. As input knowledge from the domain (and as can be seen from the extracted bubbles), we know that stable bubbles need to be attached to porous structures at some points. For the analysis, the Euclidean distance between bubble and surrounding structures is calculated to separate the bubble surface into two areas. The bubble surface area exhibiting a distance to the medium below a certain threshold is denoted as the *Connected-surface* (i.e., it is classified as being attached to porous structure). In reverse, areas with distances above the threshold (distance larger than 5 voxels) are denoted as *Free-surface*, as they can freely move and deform (e.g., expand or shrink). This threshold is used to yield robust results even in cases of small inaccuracies stemming from the segmentation process. According to our observations, *Connected-surfaces* detected with this process that only have small contact areas with the surface constitute false positives. To address this, we only count those cases in which the identified area of the *Connected-surface* is at least 20% of the total bubble surface area.

The determined *Connected-surface* areas capture crucial bubble characteristics and provide important insights for the analysis of porous structure boundary conditions. We count the number of *Connected-surfaces* for each bubble and also fit planes to every *Connected-surface* via least square optimization. The fitting planes are regarded as important features and are used in the morphology-based classification. In particular, we utilize the number of fitting planes to classify bubbles into three clusters. In $\mathscr{C}luster_1$, only one side of a bubble connects to a porous medium (i.e., there is one fitting plane). For $\mathscr{C}luster_2$, there are two contact areas of the bubble with a structure (two fitting planes), and finally, in $\mathscr{C}luster_3$, three parts of a bubble connect to a porous medium (three fitting planes). Due to the nature of the investigated experiment setup, we only identified up to three *Connected-surfaces* for a bubble in this work, but theoretically more could occur and would be detected by our approach in different setups (e.g., featuring larger bubbles). The observation of the limited bubble connectivity in our experiment already constitutes an interesting finding by itself.

4.2 Similarity of Porous Structures

Next, we propose our approach to automatically search similar structures in a porous medium. This addresses one goal of our visualization, which is to identify (and predict) all the possible locations in an unknown porous medium in which (a certain type of) bubbles can occur. Correspondence structures are regarded as boundary condition. Our algorithm could find similar local pore structures as one specific kind of cluster, which could be used for resonance effects experiments under

---

Algorithm 1 Determine the similarity of all local structures in the porous medium (discussed in Sect. 4.2).

Input:
    Exemplar bubbles set $\mathscr{D}_b$;
    Exemplar correspondence structures set $\mathscr{D}_s$;
    Desired porous dataset $\mathscr{D}_o$;
Output:
    Ensemble of nearest neighbor structure cubes $x_s \in \mathscr{X}_s$;

1: Build exemplar-structure feature set $\mathscr{F}_e$, $f_e \in \mathscr{F}_e$;
2: Build desired-structure feature set $\mathscr{F}_o$, $f_o \in \mathscr{F}_o$ in $\mathscr{D}_o$;
3: **for** each $f_e \in \mathscr{F}_e$ **do**
4:     **for** each $f_o \in \mathscr{F}_o$ **do**
5:         Compute similarity error $\delta = \|f_o - f_e\|_2$;
6:         Sort with respect to similarity error δ;
7:         Construct the nearest similar structures set $\mathscr{X}_s$, $x_s \in \mathscr{X}_s$;
8: **for** k nearest similar structures in $\mathscr{X}_s$ **do**
9:     **if** bubble occurs **then**
10:         Add bubble x_b to $\mathscr{X}_b$, $\mathscr{N}_b = \mathscr{N}_b + 1$;

---

similar boundary conditions. The individual steps of our approach are outlined in algorithm 1, and discussed in detail below.

(1) Build exemplar-structure feature set $\mathscr{F}_e$ (Line 1). The exemplar bubble set consists of the set of identified bubbles ($\mathscr{D}_b$) and their respective surrounding structures ($\mathscr{D}_s$). In this step, we aim to extract a simple representation of the porous structures featuring bubbles. For this, our algorithm first chooses the central voxel of each bubble as an anchor (colored in red in Figure 4(a)). We then sample our exemplar-structure feature cube f_e around this anchor voxel (Figure 4(b)). The size of the cube is chosen to be two times the size of the bounding box of the bubble to adequately capture the surrounding structure (like ROIs in Sect. 3). The features cubes f_e of all bubbles then constitute the exemplar-structure feature set $\mathscr{F}_e$.

(2) Build desired-structure feature set $\mathscr{F}_o$ (Line 2). We then sparsely sample the desired porous dataset $\mathscr{D}_o$ (Figure 4(c,d)), with the center voxels being colored in red. Each desired-structure feature cube f_o is generated by starting from the central sampling voxels and then incorporating neighboring voxels, which is shown in Figure 4(c). We further rotate around these center voxels in x, y and z direction to account for different structure orientations. All the feature cubes f_o constitute the desired-structure feature set $\mathscr{F}_o$, $f_o \in \mathscr{F}_o$, in which our algorithm searches for the nearest spatial structures.

(3) Calculate the similarity of exemplar-feature f_e and desired-feature f_o (Lines 3-7). The exemplar features $f_e \in \mathscr{F}_e$ are compared with every desired feature $f_o \in \mathscr{F}_o$ by calculating the sum of distances of all voxel values in one feature cube via $\delta = \|f_o - f_e\|_2$. We then sort $f_o \in \mathscr{F}_o$ in increasing order w.r.t. to their δ value. Finally, we chose the k nearest structures x_s and respectively construct nearest structure set $\mathscr{X}_s$ for each bubble capture by f_o.

(4) Identify bubble occurrence in nearest structures $\mathscr{X}_s$ (Lines 8-10). After building the nearest similar structure set $\mathscr{X}_s$, we then identify whether a bubble actually occurs in each structure $x_s \in \mathscr{X}_s$. If this is the case, we add the respective bubble x_b to $\mathscr{X}_b$.

In our implementation, to reduce the significant cost of identifying similar structures (in step **(3)** and **(4)**), we use an acceleration approach to cut down the number of expensive direct voxel block comparisons that we have to carry out. For this, we employ principle component analysis (PCA) [13], a statistical dimension reduction method that operates on the voxels in the exemplar and the desired-structure feature cube. Here, the input is the vector of voxels in the exemplar or the desired-structure feature cube. Specifically, we calculate the eigenvalues and only keep the set of largest eigenvalues that add up to around 95 percent of the total sum. For instance, for a 10^3 cube, we have a 1000-dimensional vector, which reduces down to 76 dimensions after PCA reduction. A k-d tree is employed to store this reduced representation for quickly identifying similar structures. To build the feature set

$\mathscr{F}_o$ in our experiments, we considered rotations around all axes with a $90°$ angle, and use a distance between anchor voxels of eight voxels.

4.3 Similarity of Bubble Shapes

One important aspect that we aim to study in this work is to assess what the different influence factors are that determine shape characteristics of bubbles. For this, we assess the similarity of bubbles on the basis of a combination of suitable feature descriptors which are computed on the basis of the extracted bubble meshes. Geometric feature descriptors quantitatively describe the 3D shape of bubbles in a way that is invariant to scaling and rotation. We combine different descriptors to improve their expressiveness, yet at the cost of increasing computation time. In this work, we use the shape diameter function [32], Gaussian curvature [15], and the volume surface ratio, which are among the most effective and widely used 3D geometric shape descriptors.

The Shape Diameter Function $\mathscr{D}$ is a scalar function $f : M \rightarrow \mathfrak{R}$ on the surface, where M is a manifold mesh surface defining a volumetric mesh. It expresses a measure of diameter distance at each vertex to its neighborhood vertices on mesh surface, which is able to capture the bubbles volumetric shape locally. The Gaussian Curvature $\mathscr{G}$ is the product of principal curvatures, k_1 and k_2 at each point on a surface, and with this quantifies the degree of unevenness of the bubble. The Surface-to-volume Ratio $\mathscr{R}$ simply denotes the ratio between volume and surface area of the bubble.

We quantify the difference between two bubbles on the basis of the individual differences between descriptors. The surface-to-volume ratio $\mathscr{R}$ is only a single descriptive number for the whole bubble, and we use the squared difference between them to compute the distance $\mathscr{E}_{\mathscr{R}}$. In contrast, the shape diameter function $\mathscr{D}$ and the Gaussian curvature $\mathscr{G}$ are computed per vertex of the respective mesh, and we compute normalized histograms from these values. To compare these histograms, we simply sum the squared differences of the individual bins to yield $\mathscr{E}_{\mathscr{D}}$ and $\mathscr{E}_{\mathscr{G}}$ (we use 100 histogram bins in our implementation) . With this, we then compute the distance $\mathscr{E}(\mathscr{V})$ as a weighted average of $\mathscr{E}_{\mathscr{D}}$, $\mathscr{E}_{\mathscr{G}}$ and $\mathscr{E}_{\mathscr{R}}$:

$$\mathscr{E}(\mathscr{V}) = w\mathscr{E}_{\mathscr{D}} + \mu\mathscr{E}_{\mathscr{G}} + \lambda\mathscr{E}_{\mathscr{R}} \tag{1}$$

where w, μ, λ are the weights of shape diameter function, Gaussian curvature and volume-surface ratio. In this work, we use $w = 0.5$, $\mu = 0.3$, and $\lambda = 0.2$, considering the importance of the respective characteristics in our analysis. Note that while we use these metrics in this paper for assessing similarities between bubbles only, they could also be useful for more advanced resonance effect experiments as they capture the bubble shaped in a meaningful way (akin to the simulation using bubble characteristics discussed in Sect. 6(v)).

5 REGISTRATION FOR DIRECT VISUAL COMPARISON

To visually compare bubbles in a focus+context-style visualization, we align them in a meaningful way by registering them via rigid transformations. For this, we employ the Iterative Closest Point (ICP) algorithm (e.g., [31]), a commonly used method for registration. The ICP algorithm determines a rigid-body transformation, composed of a rotation and a translation to minimize the sum of squared distances of corresponding points. These transformations are iteratively improved throughout the course of the algorithm. The quality of alignment that can be achieved depends heavily on choosing good pairs of points, in particular for the initial points that are used to determine the first, initial transformation. A popular approach is to identify the initial points using a covariance matrix (e.g., [9]). However, this cannot handle the situation very well if one object extends far beyond the other one, due to the reason that small misalignments will be significantly amplified. Therefore, while we directly use the ICP implementation distributed with MeshLab [6] in this work, we developed a customized technique for determining suitable initial points for bubble registration.

The core idea is to select points based on the fitting planes of each bubble, as they expressively not only capture shape but also CO_2 bubble morphology. For this, we take bubble characteristics into account to achieve good results for our use case. In particular, from our findings so far, we can see that we almost exclusively get bubbles with two or three fitting planes, which is why we concentrate on these cases in

---

Algorithm 2 Selection of initial geometric points for bubble and correspondence structure registration. For the sake of simplicity, we assume in the description below that a bubble is convex (i.e., there is maximally two intersections with a line), and that they are ordered such that P_1, P_2 are the ones with smallest enclosing angle in the case of three fitting planes $|P| = 3$.

1: **for** $i \in 1 \ldots |P|$ **do**
2:     $\mathscr{A}_i \leftarrow$ project *Connected-surface i* onto P_i
3:     $a_i \leftarrow$ centroid of $\mathscr{A}_i$
4:     denote $L_i = a_i + \lambda n_i$ (n_i is the normal of P_i)
5:     $v_i \leftarrow$ intersect L_i with b (use result closest to a_i)
6: Line segment $\overline{l_1, l_2} \leftarrow$ shortest distance between L_1 and L_2
7: Midpoint $l_c \leftarrow (l_1 + l_2)/2$
8: Line $M \leftarrow$ intersect P_1 and P_2
9: Line segment $\overline{m_1 m_2} \leftarrow$ project v_1 and v_2 onto M
10: Midpoint $m_c \leftarrow (m_1 + m_2)/2$
11: $v_{|P|+1} \leftarrow$ intersection of line seg. $\overline{m_c, l_c}$ with b
12: **if** $|P| = 2$ **then**
13:     $v_4 \leftarrow$ intersect L_1 with b (use result furthest from a_i)
14:     $v_5 \leftarrow$ intersect L_2 with b (use result furthest from a_i)
15: **else if** $|P| = 3$ **then**
16:     $v_5 \leftarrow$ intersect b with $l_c + \lambda n_1$ and $l_c + \lambda n_2$ (use result closest to l_c)

---

the following. The initial geometric points selection for two and three fitting planes, respectively, are illustrated using a 2D projected diagram by example in Figure 5(a & b). Details are discussed in the following by means of Algorithm 2.

Before we start, in the case of three fitting planes $|P| = 3$, we order them in a way such that (P_1, P_2) is the pair of planes with smallest enclosing angle. First of all, for each plane $P_i \in P$ for a bubble b (Line 1), we project the connected surface (from Sect. 4.1) onto P_i to create a splat $\mathscr{A}_i$ (Line 2). We then compute the centroid a_i of $\mathscr{A}_i$, and use it to define a line L_i through this point in the direction of the normal of P_i (Line 4). Then, we use L_i to determine the respective vertex v_i on the bubble surface that is close to P_i. This then constitutes a set of points that describes basic connectivity properties of the bubble.

On this basis, we then continue and compute two central positions as the basis for further computations. First, we compute the line segment that crosses the shortest distance between L_1 and L_2, and determine the respective midpoint l_c (Line 7). Second, we intersect the two fitting planes P_1 and P_2 to determine respective line M, on which then the two respective points determined so far (v_1 and v_2) are projected, yielding m_1 and m_2. We then compute the midpoint m_c between m_1 and m_2 (Line 10). With this, we compute the intersection point between l_c and m_c (Line 11). This then provides the basis for specialization, whereas we handle the cases of $|P| = 2$ and $|P| = 3$ in a different way to account for the typical properties of the shapes that we could observe in our analysis.

For $|P| = 2$ (from Line 12), we just compute the intersection of L_1 and L_2 with the bubble b again (similar to Line 5), but this time we keep the intersection points far away from the fitting planes. In addition, we identify an intersection point close to m_c to specifically capture the typical property of bubbles with two planes in that they are commonly positioned in corners (Line 14). For $|P| = 3$ (from Line 15), we just compute the final point going outward from l_c with the normals of both planes P_1 and P_2, and determine the intersection with the bubble b that is closest to l_c (Line 16).

In this work, we limit ourselves to cases with at most three fitting planes as no bubbles beyond this were identified in our data set, but our method could easily be extended to bubbles with more fitting planes by using the projection of central points of each plane onto bubble surface as initial points directly for ICP. Also, while we concentrated our discussion on two and three fitting planes, we also developed a variant for $|P| = 1$, which can be seen as a simpler variant of the $|P| = 2$ case (it is not discussed here, as it has not been used during our analysis). To demonstrate the benefits of our selection approach, we compare our
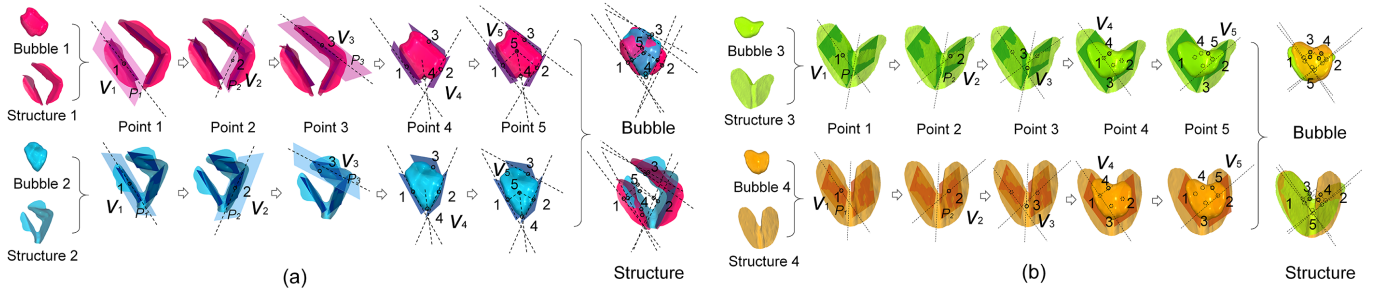
Fig. 5: Examples for our geometry-based initial point selection for (a) three and (b) two fitting planes (discussed in Sect. 5).

results below against the popular approach for ICP point selection by Gelfand et al. [9] (see Sect. 6 and Figure 8 for details).

6 VISUAL ANALYSIS OF BUBBLE FORMATION

The goal of this work is to gain more insight into CO_2 sequestration processes in a collaborative effort of visualization researchers and domain experts studying these effects. The porous media dataset we examine stems from X-ray CT scanning of a Fontainebleau sandstone core of 5 mm under confinement pressure of 20 bar. The sample was saturated with CO_2 and was injected with an initial pore pressure of 15 bar. The pressure was decreased in 0.5 bar steps, and a tomographic snapshot was taken at each point until the pore pressure was equal to the rooms pressure. In this work, we only consider the last volume of the series as we are primarily interested in the bubbles that persisted. The XCT data was recorded at the Paul Scherrer Institute TOMCAT beamline, and the final volume has a resolution of 0.65 µm per voxel and a domain size of $2560 \times 2560 \times 2160$ voxels. Each voxel contains a 16 bit value which is equivalent to the local x-ray absorption value of the sample. Our visual analysis has been carried out on a system featuring an Intel(R) Core(TM) i7-6700 CPU with 3.40 GHz, 32 GB of RAM, and an NVidia Geforce GTX1080 graphics card. Our proposed nearest spatial structure searching (Algorithm 1) requires less than one minute, and the registration method Algorithm 2 takes only a few seconds to compute. In the following, we now employ the techniques introduced above to visually analyze the data, present our findings, and discuss what insights we have gained from this (focusing on our research questions).

As a prerequisite for the evaluation below, we were able to correctly identify and locate bubbles in primarily automatic fashion, with only little user input required. Previously, this used to be a manual task that is tedious and time-consuming, so we were able to get a full picture of the present bubbles in the porous media for the first time and conduct a full analysis on this basis. *(i)* We first employ our morphology-based clustering and get an overview where bubbles form; *(ii)* we search the nearest spatial pore structure and visualize the possibility locations of potential bubble formation; *(iii)* we then identify similar bubble shapes and analyze them regarding their commonalities and differences; *(iv)* we apply our registration method for in-place, direct visual comparison and compare its effectiveness to a standard approach; *(v)* we derive the bubble size distribution and on this basis study resonance effects; *(vi)* we summarize the significance of this work for CO_2 sequestration research and discuss some limitations and directions for future work.

(i) Morphology-based Bubble Clustering

We first classify bubbles into different classes with respect to their morphology in terms of how they are connected to the surrounding porous structure (cf. Sect. 4.1). With this, we can not only start the address the questions where bubbles form (**RQ1 (bubble locations)**), but also start to asses the conditions that must be present for a stable bubble to form (**RQ3 (structure influence on bubble)**). The classification results in three clusters as can be seen in Figure 6, which is rendered using a visualization package Paraview [2]. $\mathscr{C}luster_1$, $\mathscr{C}luster_2$ and $\mathscr{C}luster_3$ connect to one, two and three structure surfaces, respectively.

In our applications, water is the wetting fluid. The first observation from the overall bubble shape is that CO_2 is acting as a wetting phase. Bubbles in $\mathscr{C}luster_1$ are difficult to create as a wetting fluid, since they

usually tend to be a very thin layer over the solid surface. Therefore, the existence of these bubbles indicates that solid surface roughness does play a role in not only the formation of gas bubbles, but also in their final shape and position. Bubbles of $\mathscr{C}luster_2$ tend to be found in corners of the pores, while bubbles in $\mathscr{C}luster_3$ commonly form bridges. The number of bubbles in $\mathscr{C}luster_1$, $\mathscr{C}luster_2$ and $\mathscr{C}luster_3$ accounts for 1.03%, 41.38% and 48.29% of all bubbles respectively. From the percentage of each cluster, we statistically find the more solid surfaces a bubble connects to, the more stable it will be. This gives a guidance of what kind of porous structures to look out for in the context of CO_2 bubble storage. Interestingly, we found that there are stable bubbles not attached to porous structure, and that also no cases with a larger number of connection points occurred (one reason for this could be the relatively small size of bubbles occurring in our experimental setup). Interestingly, the findings also show that there are numerous bubbles with a comparably complex, non-spherical geometry. The form and location of bubble formation strongly depend on the specific surface properties of the porous medium. We expect, that this will be changed completely if e.g. different types of reservoir sandstones are compared. To conclude, these results underline the need of Direct Numerical Simulations for bubble resonance effects.

Furthermore, we gained insights regarding the boundary conditions, i.e. how and where the bubbles are attached to the solid surfaces for the formulation of these Boundary Value Problems (BVPs). Pinned or attached bubbles, i.e. bubbles with kinematical boundary conditions, have different resonance frequencies (eigenmodes) compared to free non-attached bubbles. These insights could help to numerically simulate the dynamic response of bubbles. Free non-attached bubbles can be already physically analyzed and resonance properties have been calculated for the segmented size distribution, cf. Fig. 11. It could be clearly observed, that there is a frequency band around the characteristic (resonance) frequency $\bar{\omega}$ where abnormal velocity dispersion (and attenuation) occurs.

(ii) Comparing Bubble Formations in Similar Pore Structures

We now employ our approach to find similar spatial structures (Sect. 4.2, Algorithm1) in order to identify potential locations where a specific type of bubbles occurs (addressing another aspect of **RQ1 (bubble locations)**). For this, we determine the 20 most similar structure shapes for each corresponding structure and visualize all the structures color-coded with respect to similarity (Figure 7). With this, we were able to automatically analyze and predict where potential positions of (gas) bubbles are in the pore space, which allows for a potential estimate about the numbers (and locations) of bubbles in a unit cell.

This also helps to anticipate the respective acoustic properties of bubbles. The Elasto-dynamical unit cell investigations of porous materials saturated with a pore fluid and bubbles allow for the calculation of acoustic properties and therefore the dispersive characteristics (e.g. phase velocities and attenuation). When possible locations of bubbles are known, generic worst case scenarios with the maximum numbers of bubbles can be performed (highest amount of attenuation). The similarity visualization results construct a pore structure categories, which greatly enrich the ensemble for acoustic property experiments.

(iii) Geometry-based Bubble Similarity Metric

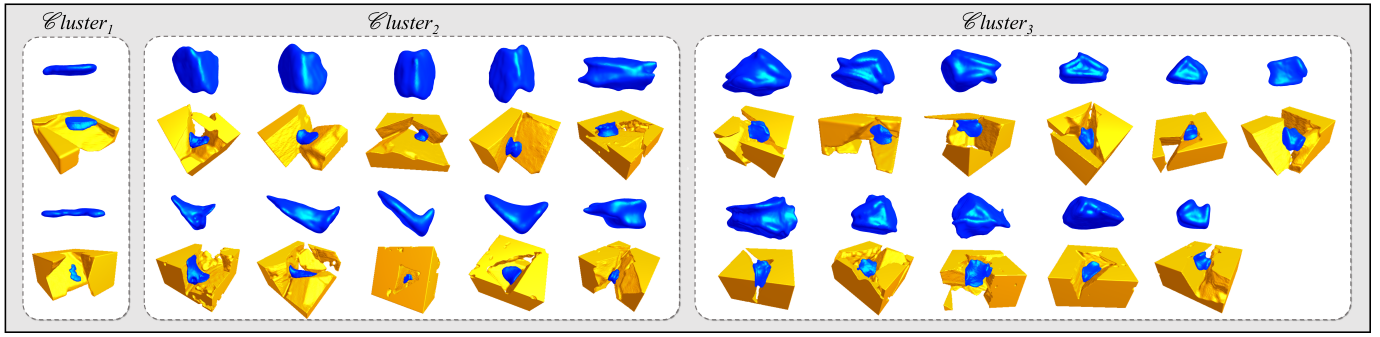For further analyzing the influence of correspondence structure on

Fig. 6: Morphology-based classification of bubbles. $Cluster_1$, $Cluster_2$, and $Cluster_3$ include the bubbles that are connected to the porous medium with one, two, and three sides, respectively. Here,we can observe that CO_2 is acting as a wetting phase. $Cluster_1$ bubbles are difficult to create as a wetting fluid, since they usually tend to be a very thin layer over the solid surface. Therefore, the existence of these bubbles indicates that solid surface roughness does play a role in not only the formation of gas bubbles, but also in their final shape and position. Bubbles of $Cluster_2$ tend to be found in corners of the pores, and $Cluster_3$ bubbles are commonly found as bridges.

(a) k-nearest structures for bubbles in $Cluster_2$

(b) k-nearest structures for bubbles in $Cluster_3$
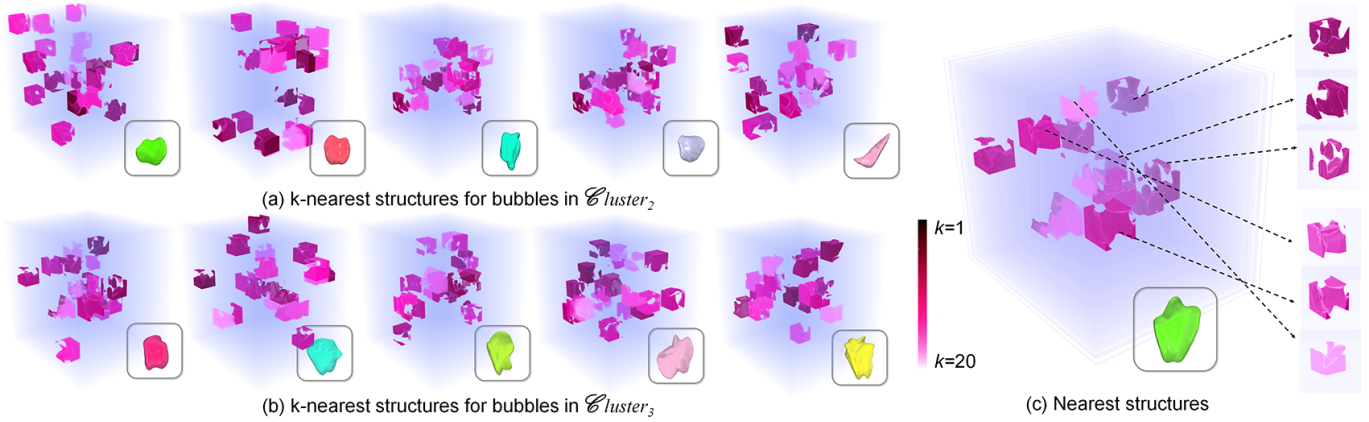
(c) Nearest structures

Fig. 7: For different porous structures in which bubbles occur, similar structures in the data set are highlighted to indicate potential locations for certain types of bubbles. In (a) and (b), the 20 most similar porous structures for one specific bubble (bottom right) are presented for bubbles in $Cluster_2$ and $Cluster_3$, respectively. (c) shows the most similar structures (top three) and the least similar structures (bottom three) for a bubble. The color map from purple to pink denotes decreasing similarity. This addresses **RQ1 (bubble locations)** and **RQ4 (bubble from structure)**, showing the potential of a pore space to sequester additional CO_2. These results also help to steer the injection fluid parameters in future experiments, and support our ongoing efforts to develop a method to predict wave attenuation from XCT dry scans.

a bubbles shape (toward **RQ3 (structure influence on bubble)**), our approach supports to observe the variation of correspondence structures that belong to similar bubbles (cf. Sect. 4.3). As a first step toward this, we applied the geometry-based bubble similarity metric to all $Clusters$. A full similarity-sorted list of bubbles in $Cluster_3$ can be found in Figure 8(a). The nearest neighbors of bubbles in each row were arranged in the order of increasing geometric error (via our geometry-based bubble similarity metric, Equation 1). For instance, $Bubble_1$ (Row No.1) and $Bubble_9$ (Row No.9) are nearest neighbors to each other. However, naturally the nearest neighbor does not have to be mutual. In particular, this is the case when shapes are relatively different with respect to all shapes. For instance, the nearest neighbor of $Bubble_3$ is $Bubble_2$, while the nearest neighbor of $Bubble_2$ is $Bubble_7$. The distance according to our metric between $Bubble_3$ to $Bubble_2$ is larger than the distance between $Bubble_7$ to $Bubble_2$, which means $Bubble_7$ is more similar to $Bubble_2$ than $Bubble_3$.

In practice, this allows us not only to look at the closest bubbles as determined by our approach from Figure 8(a) (similar or non-similar ones, depending on the analysis task), but also enables searching a cluster of similar shapes, which avoids large amounts of tedious and repetitive work and reduces human-introduced error. It further helps us with the analysis of bubbles with complex boundary conditions, as the number of simulations for bubbles in one cluster could be reduced to a "master bubble". Especially from Figure 8, we could check not only the geometrical differences of the most similar bubbles (e.g. the master bubble) but we can also analyze the difference in boundary conditions.

This constitutes an important contribution to the analysis of bubble with complex boundary conditions.

(iv) Registration for In-place, Direct Visual Comparison

On the basis of the collection of similar bubbles, we now study how bubble morphology shape variation dependends on differences of surrounding structures (**RQ3 (structure influence on bubble)**). For this, we employ our structure registration approach to enable a meaningful direct visual comparison (cf. Sect. 5). With this, we can choose a nearest neighbor bubble pair in Figure 8(a) and directly see the registration results from different views (Figure 8(b)). The comparison of two registration results of the nearest neighbor pair (Figure 8(a)) are shown in Figure 8(c). The black rectangles in the first row of Figure 8(c) show the mismatch and inappropriate registration of the standard method, making a meaningful direct comparison difficult. We also quantitatively validate the two registration methods on the basis of bubble centroids. The mean error difference of our method is 3.5 mm, while the standard method yields 7.9 mm, which is significantly larger. Moreover, results for multiple registered bubbles and structures from one central perspective are shown in Figure 9. Via the bounding boxes of the bubbles we quantitatively assess the bubble shape variation and the correspondence structure angle rotation. For example, $Bubble_1$ is larger by 18.97 % in the principle z-direction and smaller by 1.32 % and 2.62 % in the x-direction and y-direction in comparison to $Bubble_9$. The three fitting planes of $Bubble_1$ deviate by 32.4°, 6.5° and 2.9°, respectively, with respect to $Bubble_9$.
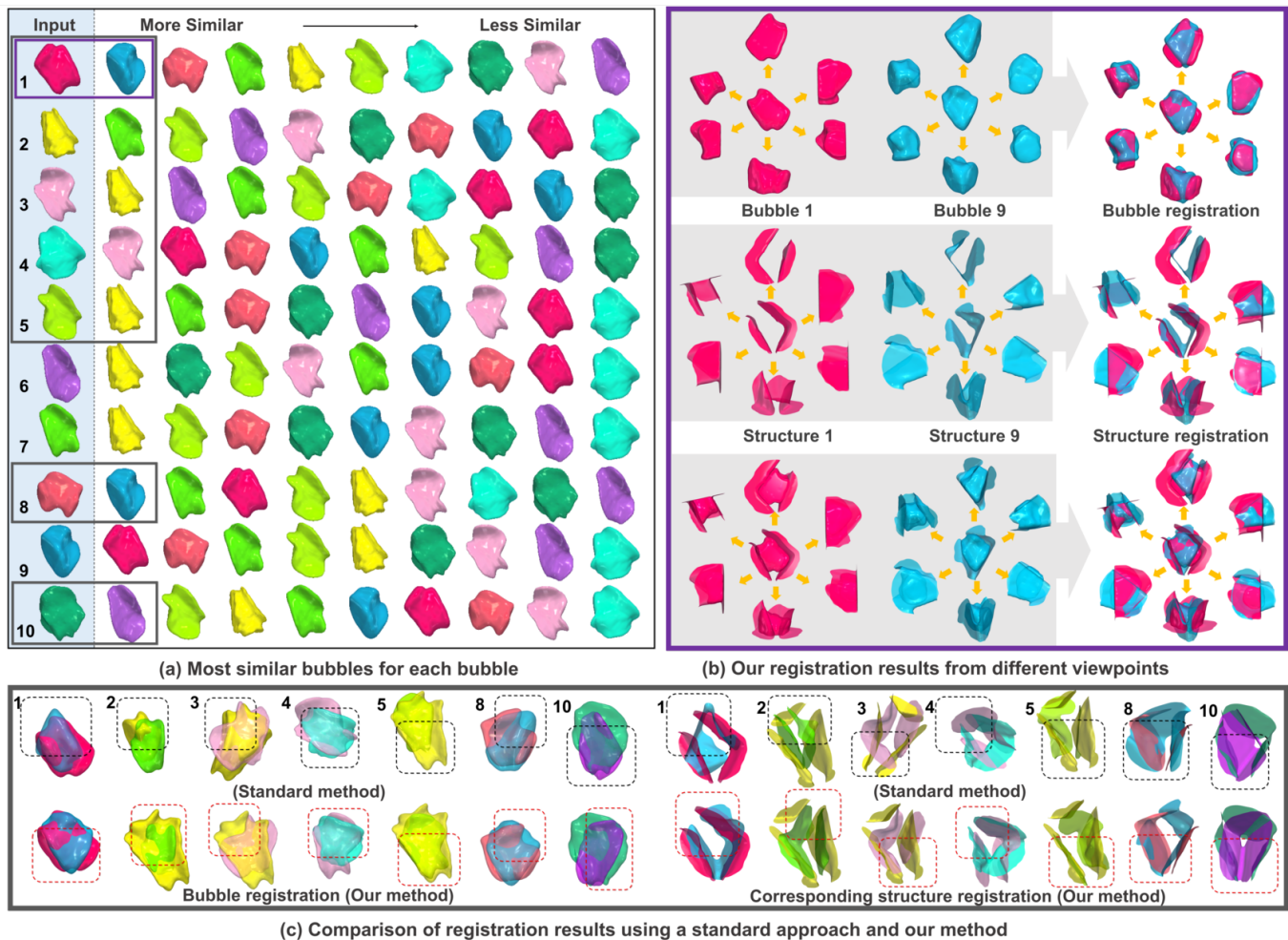
Fig. 8: Comparing bubbles to gain insights regarding underlying properties. (a) For each bubble, we automatically determine the most similar bubbles of the same morphology class. (b) We render and compare the registered results of the most similar bubble pair (e.g. 1 and 9) from different views. (c) Registration results for selected bubble pairs (gray boxes in (a)) using a standard method (dotted black box, top) and our approach (dotted red box, bottom). Dotted boxes indicate inadequate parts of the registration with the standard method. The similarity in the pore space geometry surrounding similar bubbles reinforces the idea of identifying a prototypical bubble per cluster (**RQ3**). The difference found between the bubbles can then be attributed to a scaling difference (**RQ2**).

In particular, this direct comparison of bubble and structure shape variation allows us to create a link between bubble and pore space by quantitatively assessing the shape variation of the bubble and the angle rotation of correspondence structure in pore space. From the pore morphology we would then extract bubble positions, sizes and boundary conditions. On the basis of that knowledge, we could perform in the future image-based numerical finite element calculations for the determination of bubble resonance frequencies.

(v) Bubble Size Distribution and Resonance Frequency

We could observe the bubble size distribution (e.g. in a unit cell) with quantitative values through different colors, which is directly linked to the resonance frequency of a single bubble (**RQ2 (bubble size distribution)**). We also learned that measuring and visualizing curvature is not trivial, because of the lack of a smooth curvature solution. But, what we also could learn is that mean curvature could be potentially determined well which supports the basic idea of our coarse-grained acoustic model based on simple geometries (e.g., spheres). Since we've known the bubble size distribution we could directly calculate the distribution of resonance frequencies. As all resonance frequencies directly contribute to the dispersive response of the medium such an information is very important. Assuming simplest geometries of the bubbles (spheres), these resonance or eigen-frequencies could even

been calculated analytically based on the dispersion relations derived for the model proposed in [7, 25].

We plot the phase velocity for the longitudinal wave (P-wave / compressional wave) as a function of frequency for a mixture of water with discrete gas bubbles (Figure 11). The dispersion relation has been derived in [7] where more explanations can be found. We have chosen a bubble size distribution in order to evaluate the dispersion relation according to the size distribution obtained from the XCT scans (blue solid curve). This phase velocity dispersion is compared to results based on a single bubble with the mean diameter. The influence of the bubble diameter and diameter distribution can be clearly observed. Note the distinct shift in frequency domain to lower frequencies. Further, in a certain frequency band, (from around 0.5-5 $\omega/\bar{\omega}$), a strong deviation from the lower and higher frequency limits are visible. Table 1 shows the average value of each $\mathscr{C}luster$ on volume, surface area and radius of bubbles. The mean curvatures of bubbles are shown in Figure 10. The great variation of curvature in its value due to the nature of the non-smoothness of discrete surfaces.

(vi) Significance for CO_2 Sequestration Research

The obtained visualization results allow for the first time to have a deeper insight in the formation of gas bubbles in porous media. The information is not only restricted to the morphology of the bubbles, but

Cluster	Volume (voxel)	Free-surface area	Whole-Surface area	Free-surface / Volume	Whole-surface/ Volume	Free-surface Radius	Whole-surface Radius
1	31650	3805	7548	0.1202	0.2385	48.3816	27.5144
2	155415	8634	19475	0.0556	0.1253	37.6325	37.5162
3	276123	11999	26615	0.0434	0.0964	41.6289	43.1703
Total	192384	9491	21627	0.0493	0.1124	39.9731	39.1535

Table 1: Volume, fitting surface area and radius of bubbles in $\mathscr{C}luster_1$, $\mathscr{C}luster_2$ and $\mathscr{C}luster_3$ (average values).
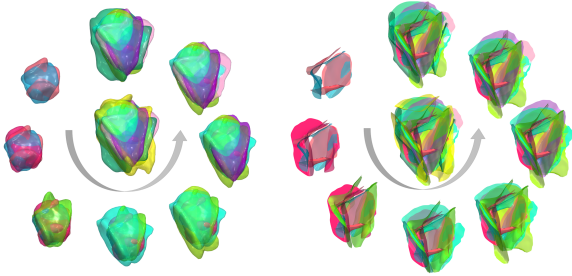

Fig. 9: Rendering of multiple registered bubbles (left) and respective structures (right) for members of $\mathscr{C}luster_3$ (color denotes $Bubble_1$ to $Bubble_{10}$ from $\mathscr{C}luster_3$). In the centers, all bubbles and corresponding structures are shown, while around them further bubbles and structures are incrementally added. This comparison reinforces the idea of a similar set of boundary conditions of the bubbles in $\mathscr{C}luster_3$ (**RQ3 (structure influence on bubble)**), since they are attached to surface planes with similar normal directions.
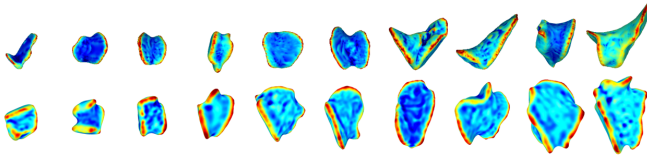

Fig. 10: Bubble curvature (from red $\hat{=}$ large to blue $\hat{=}$ small) for $\mathscr{C}luster_2$ (top) and $\mathscr{C}luster_3$ (bottom).

also includes information about the contact of the bubble to the pore surfaces. With this, detailed knowledge about boundary conditions can be obtained. It has been observed that the geometry of the bubbles is complex and therefore effective acoustical properties have to be calculated numerically. Theories for such investigations have been proposed [17, 18] and numerical investigations can, on the basis of our visualized results, be performed including the proper formulation of boundary conditions. Furthermore, as not only bubbles morphologies but also the the related pore structures have been characterized, we know now, where and how bubbles will be formed in the pore space. This knowledge from the visualization techniques helps us to pursue one goal of our research, namely the generation of generic data based on dry XCT scans which are much simpler to obtain.

7 Conclusion

In this paper, we presented a visualization approach for the back-analysis of CO_2 bubble-induced attenuation in porous rock formations. The fundamental understanding of attenuation phenomena in CO_2-water-saturated porous rock formations is of high interest during CO_2 sequestration processes. It consists of numerous components that were specifically designed for this analysis task. As a basis, we introduced customized techniques to extract CO_2 bubbles and their surrounding porous structure from XCT measurements. We then automatically classified them and put them into relation, both considering morphology and geometric features, with the goal to understand how the structure of porous medium influences the occurrence and the shape of formed bubbles. Our approach further directly supports searching for similar porous structures, which, among others, we used in order to determine certain types of structures with a high probability of containing bubbles of a certain type. We further proposed a customized registration technique considering the bubble shape as well as its points of contact to the
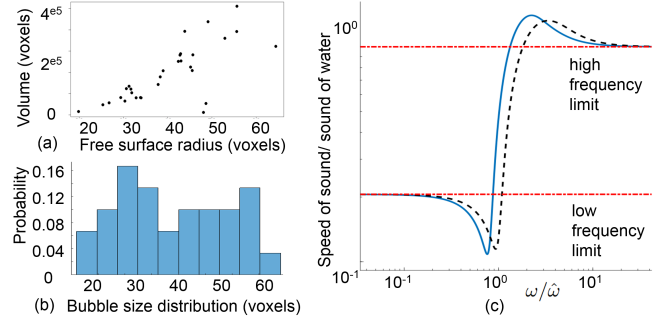

Fig. 11: (a,b) Extracted geometric measures of the bubbles encountered in our experiment. (c) These are used in a simulation of a frequency-dependent velocity of a water-gas bubble-mixture as a function of normalized angular frequency ($\hat{\omega}$ denotes the resonance frequency). The blue curve depicts the results with our extracted values (the distributions from (a,b)), while the dashed curve just uses respective mean values instead. A strong frequency shift can be seen in the logarithmic scale, underlining the importance of using measured values from actual bubbles and not just approximations.

porous media surface that allowed us to directly compare bubbles and their structures visually. With our quantitative extraction of geometric bubble features, we further supported the analysis, and laid the foundation for creating a physical model to explain characteristics of interest in future work. Most importantly, we demonstrated that our approach was successfully used to answer several research questions in the domain, toward them main goal to identify critical seismic characteristics of fluid-saturated rock that govern its capability to store CO_2.

Apart from the different directions we want to explore in CO_2 sequestration research, there are also several aspects linked to this that we aim to improve with respect to our techniques. In this regard, most importantly, the quality of the segmentation has an impact on all subsequent steps in our pipeline and naturally our analysis. This is why we aim to explore further directions on how to improve the results, and eventually even yielding a method that can manage to do this reliably without expert user interaction. This would especially be an important basis for processing time-dependent experiment data as well as ensembles, which we plan to do in future work. While we employ a couple of acceleration techniques in the identification of similar porous structures, we require certain sampling gaps to finish in an adequate amount of time, and we will work on improvements of our techniques to achieving this quickly in a dense fashion (i.e., a distance between anchors of one voxel and small variations in rotation angles) . Finally, with the plan to do a larger variety of experiments, we will need most probably encounter cases with more than three fitting planes for a bubble, and we plan to generalize our approach in this regard accordingly (most prominently, this concerns our approach for the registration of bubbles).

REFERENCES

[1] M. Andrew, B. Bijeljic, and M. J. Blunt. Pore-scale contact angle measurements at reservoir conditions using x-ray microtomography. *Advances in Water Resources*, 68:24 – 31, 2014. doi: 10.1016/j.advwatres.2014.02.014

[2] U. Ayachit. The paraview guide: a parallel visualization application. 2015.

[3] L. Bavoil, S. P. Callahan, P. J. Crossno, J. Freire, C. E. Scheidegger, C. T. Silva, and H. T. Vo. Vistrails: enabling interactive multiple-view visualizations. In *VIS*, pp. 135–142. IEEE, 2005. `doi:10.1109/VISUAL.2005.1532788`.

[4] J. Beyer, M. Hadwiger, and H. Pfister. State-of-the-art in gpu-based large-scale volume visualization. *Comput. Graph. Forum*, 34:13–37, 2015.

[5] M. Blunt, F. J. Fayers, and F. M. Orr Jr. Carbon dioxide in enhanced oil recovery. *Energy Conversion and Management*, 34(9-11):1197–1204, 1993.

[6] P. Cignoni, M. Callieri, M. Corsini, M. Dellepiane, F. Ganovelli, and G. Ranzuglia. Meshlab: an open-source mesh processing tool. In *Eurographics Italian Chapter Conference*, vol. 2008, pp. 129–136, 2008.

[7] M. Frehner, H. Steeb, and S. M. Schmalholz. Wave Velocity Dispersion and Attenuation in Media Exhibiting Internal Oscillations. In A. Petrin, ed., *Wave Propagation in Materials for Modern Applications*, pp. 455–476. INTECH, Croatia, 2010.

[8] D. Furukawa, A. Shimizu, and H. Kobatake. Automatic liver segmentation method based on maximum a posterior probability estimation and level set method. *3D Segmentation in The Clinic: A Grand Challenge*, 117, 2007.

[9] N. Gelfand, L. Ikemoto, S. Rusinkiewicz, and M. Levoy. Geometrically stable sampling for the icp algorithm. In *3-D Digital Imaging and Modeling, 2003. 3DIM 2003. Proceedings. Fourth International Conference on*, pp. 260–267. IEEE, 2003.

[10] S. Grau, E. Vergés, D. Tost, and D. Ayala. Exploration of porous structures with illustrative visualizations. *Computers & Graphics*, 34(4):398–408, 2010.

[11] A. Gyulassy, M. Duchaineau, V. Natarajan, V. Pascucci, E. Bringa, A. Higginbotham, and B. Hamann. Topologically clean distance fields. *IEEE T. Vis. Comput. Gr.*, 13:1432–1439, 2007.

[12] C. Heinzl and S. Stappen. Star: Visual computing in materials science. In *Computer Graphics Forum*, vol. 36, pp. 647–666. Wiley Online Library, 2017.

[13] A. Hertzmann, C. E. Jacobs, N. Oliver, B. Curless, and D. H. Salesin. Image analogies. In *Proceedings of the 28th annual conference on Computer graphics and interactive techniques*, pp. 327–340. ACM, 2001.

[14] M. Hilaga, Y. Shinagawa, T. Kohmura, and T. L. Kunii. Topology matching for fully automatic similarity estimation of 3d shapes. pp. 203–212. ACM, 2001.

[15] J. J. Koenderink and A. J. Van Doorn. Surface shape and curvature scales. *Image and vision computing*, 10(8):557–564, 1992.

[16] J. Krüger, J. Schneider, and R. Westermann. Clearview: An interactive context preserving hotspot visualization technique. *IEEE T. Vis. Comput. Gr.*, 12(5):941–948, 2006. doi: 10.1109/TVCG.2006.124

[17] P. S. Kurzeja and H. Steeb. Variational formulation of oscillating fluid clusters and oscillator-like classification. i. theory. *Physics of Fluids*, 26(4):042106, 2014.

[18] P. S. Kurzeja and H. Steeb. Variational formulation of oscillating fluid clusters and oscillator-like classification. ii. numerical study of pinned liquid clusters. *Physics of Fluids*, 26(4):042107, 2014.

[19] K. S. Lackner. A guide to CO_2 sequestration. *Science*, 300(5626):1677–1678, 2003.

[20] C. Li, C. Xu, C. Gui, and M. D. Fox. Distance regularized level set evolution and its application to image segmentation. *IEEE transactions on image processing*, 19(12):3243–3254, 2010.

[21] S. Lindholm, D. Jnsson, C. Hansen, and A. Ynnerman. Boundary aware reconstruction of scalar fields. *IEEE T. Vis. Comput. Gr.*, 20(12):2447–2455, 2014. doi: 10.1109/TVCG.2014.2346351

[22] W. E. Lorensen and H. E. Cline. Marching cubes: A high resolution 3d surface construction algorithm. In *ACM siggraph computer graphics*, vol. 21, pp. 163–169. ACM, 1987.

[23] G. Mavko, T. Mukerji, and J. Dvorkin. *The Rock Physics Handbook, Second Edition*. Cambridge University Press, Cambridge, UK, 2009.

[24] J. S. Meredith and H. Childs. Visualization and analysis-oriented reconstruction of material interfaces. *Comput. Graph. Forum*, 29(3):1241–1250, 2010. doi: 10.1111/j.1467-8659.2009.01671.x

[25] M. Minnaert. Xvi. on musical air-bubbles and the sounds of running water.

[26] R. Osada, T. Funkhouser, B. Chazelle, and D. Dobkin. Shape distributions. *ACM Trans. Gr.*, 21(4):807–832, 2002.

[27] P. Penas-López, S. Moreno, A. M. Soto, M. Parrales, D. V. der Meer, D. Lohse, and J. J. Rodríguez-Rodríguezguez-Rodríguez. The history effect on bubble growth and dissolution. part 2. experiments and simulations of a spherical bubble attached to a horizontal flat plate. *Journal of Fluid Mechanics*, 820:479–510, 2016.

[28] P. Penas-López, M. Parrales, J. Rodríguez-Rodríguez, and D. V. der Meer. The history effect in bubble growth and dissolution. part 1. *Journal of Fluid Mechanics*, 800:180–212, 2016.

[29] I. Prilepov, H. Obermaier, E. Deines, C. Garth, and K. I. Joy. Cubic gradient-based material interfaces. *IEEE T. Vis. Comput. Gr.*, 19(10):1687–1699, 2013. doi: 10.1109/TVCG.2013.16

[30] A. Reh, C. Gusenbauer, J. Kastner, M. E. Gröller, and C. Heinzl. Mobjects–a novel method for the visualization and interactive exploration of defects in industrial xct data. *IEEE T. Vis. Comput. Gr.*, 19(12):2906–2915, 2013.

[31] S. Rusinkiewicz and M. Levoy. Efficient variants of the icp algorithm. In *3-D Digital Imaging and Modeling, 2001. Proceedings. Third International Conference on*, pp. 145–152. IEEE, 2001.

[32] L. Shapira, A. Shamir, and D. Cohen-Or. Consistent mesh partitioning and skeletonisation using the shape diameter function. *The Visual Computer*, 24(4):249, 2008.

[33] G. C. Sharp, S. W. Lee, and D. K. Wehe. Icp registration using invariant features. *IEEE Transactions on Pattern Analysis and Machine Intelligence*, 24(1):90–102, 2002.

[34] A. Smart. Microscopic bubbles sap seismic waves' strength. *Physics Today*, 68:14–16, 2015.

[35] N. Tisato, B. Quintal, S. Chapman, Y. Podladchikov, and J.-P. Burg. Bubbles attenuate elastic waves at seismic frequencies: First experimental evidence. *Geophys. Res. Lett.*, 42:3880–3887, 2015.

[36] F. Tombari, S. Salti, and L. Di Stefano. Unique signatures of histograms for local surface description. pp. 356–369, 2010.

[37] D. Ushizima, D. Morozov, G. Weber, A. Bianchi, J. Sethian, and E. Bethel. Augmented topological descriptors of pore networks for material science. *IEEE T. Vis. Comput. Gr.*, 18:2041–2050, 2012.

[38] I. Viola, A. Kanitsar, and M. E. Gröller. Importance-driven volume rendering. In *Proceedings of the Conference on Visualization '04*, VIS '04, pp. 139–146. IEEE Computer Society, Washington, DC, USA, 2004. . doi: 10.1109/VISUAL.2004.48

[39] M. Voltolini, T.-H. Kwon, and J. Ajo-Franklin. Visualization and prediction of supercritical CO_2 distribution in sandstones during drainage: An in situ synchrotron x-ray micro-computed tomography study. *International Journal of Greenhouse Gas Control*, 66:230 – 245, 2017. doi: 10.1016/j.ijggc.2017.10.002

[40] J. Weissenböck, A. Amirkhanov, W. Li, A. Reh, A. Amirkhanov, E. Gröller, J. Kastner, and C. Heinzl. Fiberscout: An interactive tool for exploring and analyzing fiber reinforced polymers. In *Visualization Symposium (PacificVis), 2014 IEEE Pacific*, pp. 153–160. IEEE, 2014.

[41] M. L. Wu and V. Popescu. Multiperspective focus and context visualization. *IEEE T. Vis. Comput. Gr.*, 22(5):1555–1567, 2016. doi: 10.1109/TVCG.2015.2443804

[42] Z. Xue and T. Ohsumi. Seismic wave monitoring of CO_2 migration in water-saturated porous sandstone. *Exploration Geophysics*, 35(1):25–32, 2004.

[43] Y. Zhang, M. Brady, and S. Smith. Segmentation of brain mr images through a hidden markov random field model and the expectation-maximization algorithm. *IEEE transactions on medical imaging*, 20(1):45–57, 2001.

The London, Edinburgh, and Dublin Philosophical Magazine and Journal of Science, 16(104):235–248, 1933.